A bio-inspired and switchable H^+/OH^- ion-channel for room temperature exhaled CO_2 chemiresistive sensing

Chen, Honghao; Lu, Ruofei; Gao, Yixun; Yue, Xiaorui; Yang, Haihong; Li, Hao; Lee, Yi Kuen; French, Paddy J.; Wang, Yao; Zhou, Guofu

DOI
10.1039/d3ta04685k

Publication date
2023

Document Version
Final published version

Published in
Journal of Materials Chemistry A

Journal of Materials Chemistry A

ROYAL SOCIETY OF CHEMISTRY

PAPER

View Article Online
View Journal | View Issue

Cite this: J. Mater. Chem. A, 2023, 11, 21959

A bio-inspired and switchable H^+/OH^- ion-channel for room temperature exhaled CO_2 chemiresistive sensing†

Honghao Chen,[ab] Ruofei Lu,[ab] Yixun Gao,[ab] Xiaorui Yue,[ab] Haihong Yang,[c] Hao Li,[ab] Yi-Kuen Lee,[de] Paddy J. French,[f] Yao Wang *[ab] and Guofu Zhou[ab]

Received 6th August 2023
Accepted 22nd September 2023

DOI: 10.1039/d3ta04685k

rsc.li/materials-a

Inspired by the CO_2-induced reversible activation mechanism of the slow anion channel 1 (SLAC1) in plant stomatal guard cells during plant photosynthesis, we designed and prepared a CO_2- switchable H^+/OH^- ion channel (CSPH ion channel). A high-performance chemiresistive room temperature CO_2 sensor has been prepared based on this CSPH ion channel. The obtained CO_2 room temperature sensor γ-CD-MOF@RhB exhibits high sensitivity ($R_g/R_0 = 1.50$, 100 ppm), excellent selectivity, good stability (less than 5% reduction in 30 days response value), and 99.96% consistency with commercial infrared CO_2 meter. The practical limit of detection (pLOD) of the γ-CD-MOF@RhB sensor reaches 10 ppm at room temperature toward CO_2, which is the lowest for reported MOF-derived chemiresistive room temperature CO_2 sensors so far. Ion conduction mechanism studies have shown that the CSPH ion channel behaves as a CO_2-switchable H^+/OH^- ion channel with a switching point of approximately 60 000 ppm CO_2. As an application attempt, the fabricated low pLOD CO_2 sensor has been used for human exhaled CO_2 detection to compare CO_2 concentration in the breath of individuals before and after exercise and COVID-19. It was also logically indicated that the average concentration of human exhaled CO_2 after COVID-19 recovery is different for undiseased subjects.

Introduction

The content of carbon dioxide (CO_2) in air is about 400 ppm, and when the CO_2 content in indoor air exceeds 1000 ppm, it can cause discomfort to the human body.[1] Therefore, CO_2 sensors are widely adopted to monitor CO_2 concentrations in enclosed spaces, such as indoor rooms, space stations, and submarines.[2,3] On the other hand, CO_2 is present in large quantities in human exhaled breath (4%, approximately 40 000 ppm), and the fractional exhaled carbon dioxide ($FeCO_2$) contains a wealth of physiological information that can be used to monitor human health.[4,5] Hence, it is significant to detect CO_2 below 100 000 ppm for both indoor air monitoring and human exhaled breath medical tests.

In clinical practice, the use of monitoring end-tidal CO_2 ($EtCO_2$) is increasing in emergency situations, such as mechanical ventilation, programmed sedation, analgesia, lung disease, heart failure, shock, metabolic disorders, and trauma.[6,7] Recent publications have reported that carbon dioxide output (V_{CO2}) is an important index of cardiopulmonary exercise testing (CPET) for the follow-up assessment of cardiopulmonary function after COVID-19 rehabilitation.[8–10] However, these assessments usually need long operating times (>30 min), bulky spectra equipment, and professional analysis, which is inconvenient for outdoor $FeCO_2$ detection. The traditional detection methods of CO_2 include infrared spectroscopy,[11,12] gas chromatography,[13] photoacoustic spectroscopy,[14] and fluorescence method.[15,16] All these methods are restricted for real-time and on-site outdoor exhaled CO_2 detection due to the high cost, complex operation, and poor portability of their instruments. Therefore, a different low-power, miniaturized, low-cost, and

[a]Guangdong Provincial Key Laboratory of Optical Information Materials and Technology & Institute of Electronic Paper Displays, South China Academy of Advanced Optoelectronics, South China Normal University, Guangzhou 510006, P. R. China. E-mail: wangyao@m.scnu.edu.cn

[b]National Center for International Research on Green Optoelectronics, South China Normal University, Guangzhou 510006, P. R. China

[c]Department of Thoracic Oncology State Key Laboratory of Respiratory Diseases, The First Affiliated Hospital of Guangzhou Medical University, Guangzhou 510006, P.R. China

[d]Department of Mechanical & Aerospace Engineering, Hong Kong University of Science and Technology, Clear Water Bay, Kowloon, Hong Kong Special Administrative Region

[e]Department of Electronic & Computer Engineering, Hong Kong University of Science and Technology, Clear Water Bay, Kowloon, Hong Kong Special Administrative Region

[f]BE Lab, Faculty EWI, Delft University of Technology, Delft 2628CD, The Netherlands

† Electronic supplementary information (ESI) available: The characterizations, including FT-IR, XPS, Fluorescence spectrum, responseresponse curve for humidity effects, pH measurement, comparison of this sensor with a commercial IR CO_2 meter and real-time response testing, details of the calculation of proton conductivity (σ) and activation energy (E_a), video of our sensors compared to commercial infrared CO_2 meters (Video 1), real-time detection video of the sensor (Video 2). See DOI: https://doi.org/10.1039/d3ta04685k

convenient CO_2 sensor is still urgently demanded for human exhaled CO_2 detection.

Recently, the chemiresistive CO_2 sensor has attracted the attention of researchers because of its portability, miniaturization, and low energy consumption. As we know, CO_2 sensing material is the core of a chemiresistive CO_2 sensor. Most CO_2 chemiresistive sensing materials are currently metal oxide semiconductors (MOSs), which not only have poor stability and sensitivity but also require high operating temperatures (typically >100 °C), causing high energy consumption and safety risks.[17,18]

Different from MOSs, metal–organic frameworks (MOFs) have been found as a potential CO_2 sensing material owing to their high-porosity structure, excellent physical adsorption ability, and diverse structures. In 2010, Stoddart *et al.* reported that γ-cyclodextrin-MOF-2 (γ-CD-MOF-2) could be used for CO_2 electrochemical sensing,[19–21] which provides a new strategy for the design and fabrication of ion conduction-based CO_2 sensors. Unfortunately, due to the nature of proton conduction in γ-CD-MOFs, it remains challenging to detect CO_2 with concentrations below 100 000 ppm.[22] It is because proton conduction in γ-CD-MOF depends on the CO_2-induced blockage of the triangular-shaped *β*-windows in the γ-CD-MOF,[22,23] which will hardly happen when CO_2 concentration is below 100 000 ppm. Hence, a different ion conduction mechanism must be employed for the detection of CO_2 with concentrations below 100 000 ppm.

It is well known that a mechanism exists in plant photosynthesis to reversibly activate the slow anion channel 1 (SLAC1) in stomatal guard cells *via* CO_2 induction.[24–26] Inspired by this different ion conduction mechanism, the low-concentration CO_2 detection is expected to be achieved using γ-CD-MOF to construct SLAC1-mimic artificial anion channels. To construct such an artificial anion channel, encapsulation of a guest ion source molecule in the cavity of γ-CD-MOF is a reasonable strategy to increase anions. Herein, rhodamine B (RhB) is selected as an ideal anion source, considering that the tertiary amine of RhB will react with water and release a large amount of hydroxide ions.[27] More importantly, the hydroxide ion can reversibly interact with CO_2, implying its potential for building a CO_2-switchable ion channel.[28] Therefore, it is proposed in this study that SLAC1-mimic artificial CO_2-switched anion channels could be constructed *via* encapsulating RhB in γ-CD-MOF and utilized to realize low-concentration room temperature CO_2 sensing.

As proposed above, in this study, RhB was first encapsulated in γ-CD-MOF by the host-guest supramolecular interaction,[29,30] then a bio-inspired switchable H^+/OH^- ion-conducting channel (CSPH ion channel), that is, a SLAC1-mimic artificial hydroxide ion-conduction channel of γ-CD-MOF@RhB was constructed for room temperature CO_2 sensing. CO_2 is used as a switch to control the opening and closing of the H^+/OH^- ion channel. Subsequently, the CSPH ion channel was integrated into the interdigital electrodes (IDEs) to obtain a room temperature CO_2 sensor (CSPH ion channel-based sensor). The CSPH ion channel CO_2 sensor has been successfully applied to assess cardiopulmonary function for humans by detection of exhaled CO_2. The CO_2 sensing mechanism of the CSPH ion channel has also been systematically investigated. This work provides a deeper understanding of SLAC1 in plants and offers a new strategy for developing room-temperature chemiresistive CO_2 sensors based on bionic artificial CO_2-switched ion channels.

Experimental section

Preparation of γ-CD-MOF, γ-CD-MOF@RhB, γ-CD-MOF@TMRM, and γ-CD-MOF@FL

γ-Cyclodextrin (99%) and rhodamine B (RhB, 99%) were purchased from Innochem, tetramethyl rhodamine methyl ester (TMRM, 98%) was purchased from TCI. Fluorescein (FL, 99%) was purchased from Macklin, and potassium hydroxide (KOH, 99%) was purchased from Sigma-Aldrich. In order to prepare γ-CD-MOF, the reported method is adopted and slightly improved.[19–21] First, add an appropriate amount of γ-cyclodextrin and potassium hydroxide (1 : 8 molar ratio) in a 20 mL glass bottle containing 5 mL of deionized water and filter the undissolved impurities with 0.45 μm filter membrane after 30 min of ultrasound. Then, place the glass vial in a larger beaker containing 20 mL of methanol and steam diffusion for 14 days to obtain γ-CD-MOF solid particles. Then, filter out the mother liquor and wash it with methanol three times before vacuum drying. The obtained cubic nanoparticles are used for characterization.

For γ-CD-MOF@RhB, γ-CD-MOF@TMRM, and γ-CD-MOF@FL, the co-crystallization method is adopted.[29–31] First, add an appropriate amount of γ-cyclodextrin and potassium hydroxide (1 : 8 molar ratio) into a 20 mL glass bottle containing 5 mL of deionized water, add a certain proportion of RhB, TMRM or FL, and filter the undissolved impurities with a 0.45 μm filter membrane after 30 min of ultrasound. Then, place the glass vial in a larger beaker containing 20 mL of methanol and steam diffusion for 14 days to obtain γ-CD-MOF@RhB, γ-CD-MOF@TMRM, or γ-CD-MOF@FL solid particles. Then, filter out the mother liquor and wash it with methanol three times before vacuum drying. The obtained cubic nanoparticles are used for characterization.

Sensor fabrication and performance measurements

The preparation process of the CO_2 sensor is similar to our previous report.[31–34] Briefly, 5 μL of sensing material dispersion (0.1 mg μL^{-1}) was drop-coated on interdigital electrodes (IDEs) and dried at 50 °C for 30 min. The resistance change of the prepared sensor was recorded with a Keithley 2450 source meter (Tektronix, USA). 1 000 000 ppm dry CO_2 target gas is purchased from Dalian Special Gas Company. A 1 L sealed test chamber is used as the test environment, and the humidity control dynamic gas distribution system (DGL-III, ELITE TECH. China) is used to configure a certain humidity background gas (5–70% RH, N_2) for the sealed test chamber. All measurements are conducted at room temperature (25 ± 2 °C). During the test, IDEs are placed in a sealed test chamber containing nitrogen with a certain humidity. After the baseline is stabilized, different volumes of dry CO_2 are injected to obtain the

resistance changes of the sensor under different concentrations of CO_2. Then, IDEs are placed in another test chamber containing nitrogen with a certain humidity for recovery. Volatile gases such as ethanol and acetone can be produced by heating the corresponding volatile compounds in the heating plate. Here, the response value is defined as $R = R_g/R_0$, where R_g is the resistance value after injecting the target gas, and R_0 is the baseline resistance value. Response time and recovery time are defined as 90% of the time of a full response or a full recovery, respectively.

Characterization of materials

The crystal structure of the prepared material was characterized by a powder X-ray diffraction instrument (XRD, D8 Advance, Bruker, Germany) with Cu as the incident radiation. Fourier transform infrared spectrophotometer (FT-IR, Vertex 70, Bruker, Germany) is used to identify the chemical groups of materials. The fluorescence spectrum (FL, RF-6000, Shimadzu, Japan) is used to measure the content of fluorophore (RhB, TMRM, FL). The element content was determined by X-ray photoelectron spectroscopy (XPS, AXIS Supra, Shimadzu, Japan). The morphology and energy dispersive X-ray spectrum (EDX mapping) of the prepared samples were analyzed by field emission electron scanning microscopy (FESEM, Quanta 250 FEG, USA). The samples were pretreated for 12 h under vacuum at 50 °C using the standard degassing station on the Mac instrument, and then the samples were subjected to nitrogen adsorption–desorption test using a 4-station fully automated Specific Surface Area Analyzer of the Micromeritics APSP 2460 model of the U.S.A. under the condition of 77 K. The nitrogen adsorption–desorption isothermal curves were obtained when the instrument had finished analyzing the samples to obtain the total specific surface area of the materials by the BET method.

Measurements of proton conductivity (σ) for MOF sheet

The proton conductivity of the material was measured by the electrochemical impedance spectrometer. Briefly, the γ-CD-MOF@RhB solid was powdered and then pressed into a circular sheet. The diameter and thickness of the circular sheet are measured by a digital caliper (diameter $d = 12.36$ mm, thickness $l = 0.72$ mm). Next, the two sides of the circular sheet are connected to the electrodes of the electrochemical impedance spectrometer and placed in a thermostatic oven. The frequency of impedance spectrum test conditions is 0.01 Hz–1 MHz, the amplitude voltage is 0.05 V, and the test temperature is 30–60 °C.

Measurements of electrodynamic force (EMF) for MOF sheet

Before EMF is measured, it is heated at 80 °C for 5 h and then connected to the electrochemical workstation. Blow in dry nitrogen on one side of the circular sheet and humidity gas on the other side. At this time, the open-circuit voltage is the EMF value. The second step is to put the sheet in a 1 L sealed test chamber and blow in the CO_2 gas stream for 15 min (50 mL min^{-1}). Then, the EMF of the CO_2-treated sheet can be measured. Finally, dry the sheet at 80 °C for 60 min and measure the EMF again to obtain a complete simulation of the CSPH ion conduction channel.

Comparison with commercial IR meter and measurement of human exhalation

The commercial IR CO_2 meter (AZ7755, Hengxin, Taiwan, China), with an accuracy of ±50 ppm ± 5%, is placed in a 5 L sealed test chamber. Calibration is required in a 5 L test chamber before testing. When different concentrations of CO_2 are injected, the corresponding readings are displayed, and the response time is about 13 min.

As for the detection of human exhalation, first of all, human exhalation is collected in a 1 L aluminum foil gas collecting bag. In order to avoid the influence of humidity, exhalation is injected into a drying device containing blue silica gel before measurement (50 mm × 100 mm, YuXin, China) and confirm whether the water absorption capacity of silica gel reaches saturation by observing the color. Then, the dried exhaled gas is used for CO_2 measurement.

Results and discussion

Fabrication of gas sensing materials and sensors

Fig. 1 shows the preparation process of the CSPH ion channel chemiresistive sensor. Briefly, a certain amount of RhB, γ-cyclodextrin, and potassium hydroxide is added to the vial containing deionised water, and the γ-CD-MOF solid cubic nanoparticles loading the RhB in the γ-CD cavity (γ-CDMOF@RhB) can be generated by the co-crystallisation method. Under the influence of the size effect, both the γ-CD-MOF cube void and the γ-CD cavity can be loaded with RhB, while γ-CD-MOFs loaded with RhB only in the γ-CD cavity can be obtained using the *in situ* co-crystallisation method, which is attributed to the strong host–guest interaction between the γ-CD cavity and RhB.[29] Subsequently, γ-CD-MOF@RhB was integrated into the interdigital electrode (IDE) by the drop-casting method, resulting in a chemiresistive sensor based on the CSPH ion channel. To verify the positive effect of external RhB in γ-CDMOF@RhB, γ-CD-MOF@TMRM (tetramethylrhodamine methyl ester) and γ-CD-MOF@FL (fluorescein) were also prepared by a similar method.

Characterization of gas-sensing materials

As shown in Fig. 2a–d, scanning electron microscopy (SEM) and transmission electron microscopy (TEM) show the cubic morphology of γ-CD-MOF before and after encapsulation by RhB. High-angle annular dark-field scanning transmission electron microscopy (HAADF-STEM) was used to analyse the detailed composition and morphology of the material (Fig. 2e). The TEM elemental mapping results show a uniform distribution of C, N, O, and K in the material and also indicate a low loading of RhB (Fig. 2f–i). Powder X-ray diffraction (PXRD) data showed that the γ-CD-MOF@RhB, γ-CD-MOF@TMRM, and γ-CD-MOF@FL retained the original structure of γ-CD-MOF (Fig. 3a). Fourier transform infrared spectroscopy (FT-IR) was

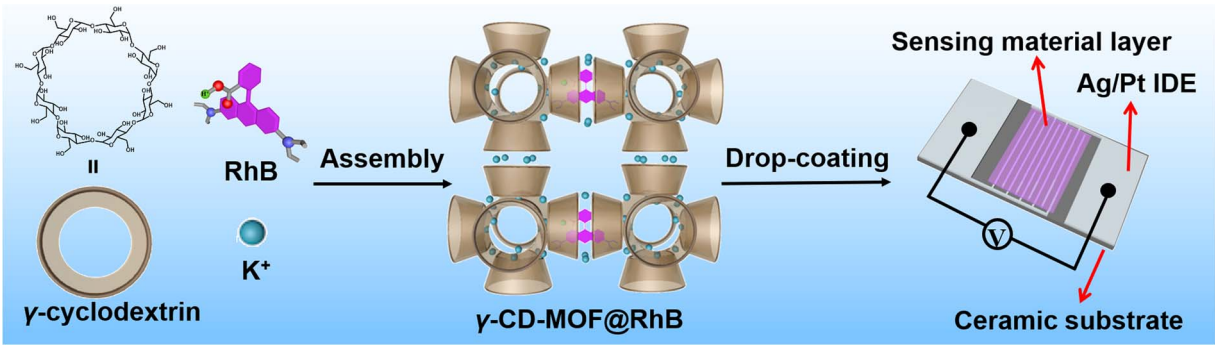

Fig. 1 Preparation process of the chemiresistive sensor.

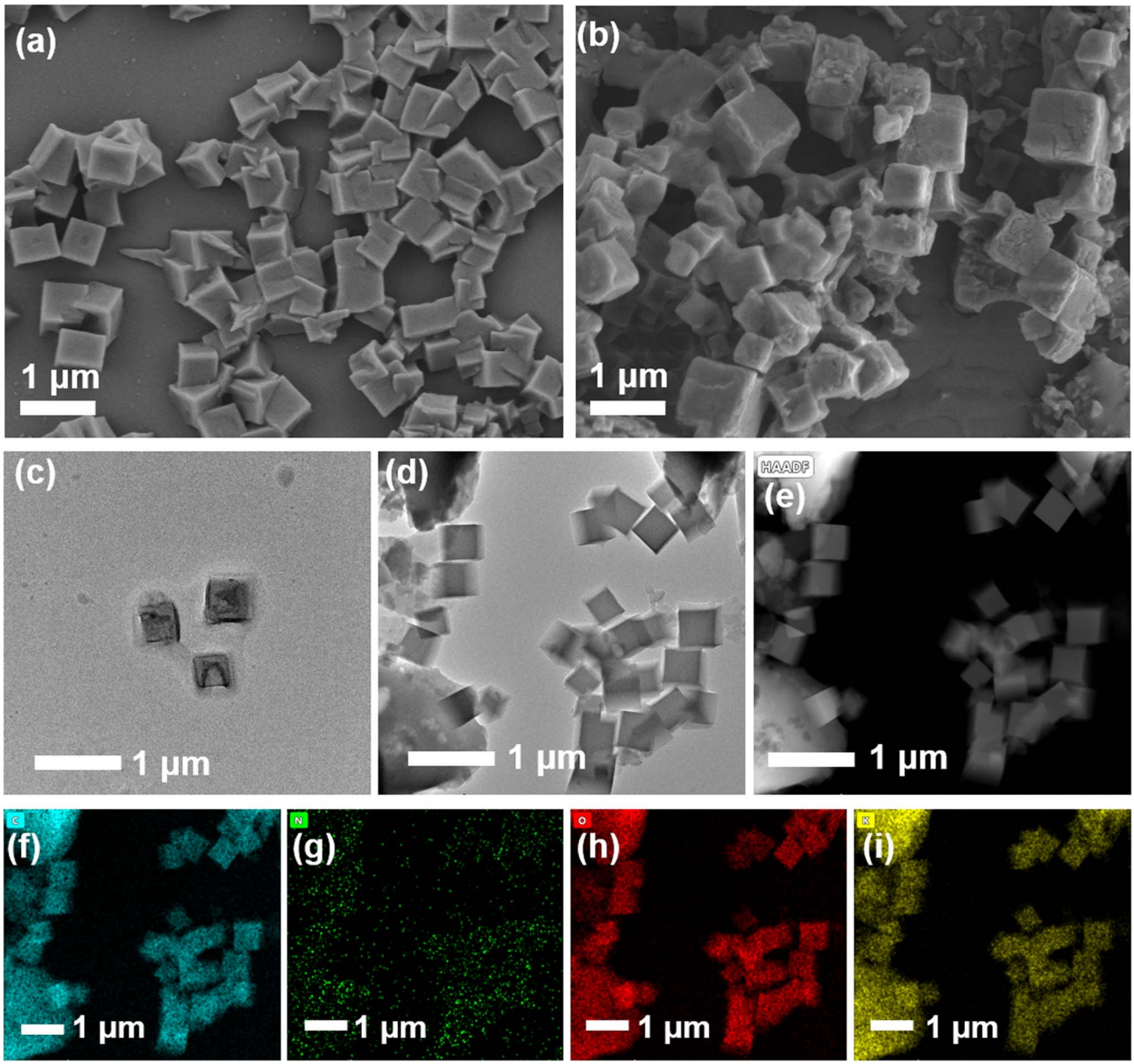

Fig. 2 (a and b) SEM images of γ-CD-MOF and γ-CD-MOF@RhB. (c and d) TEM mages of γ-CD-MOF and γ-CD-MOF@RhB. (e) HAADF-STEM images of γ-CD-MOF@RhB, and (f–i) TEM elemental mapping images of γ-CD-MOF@RhB.

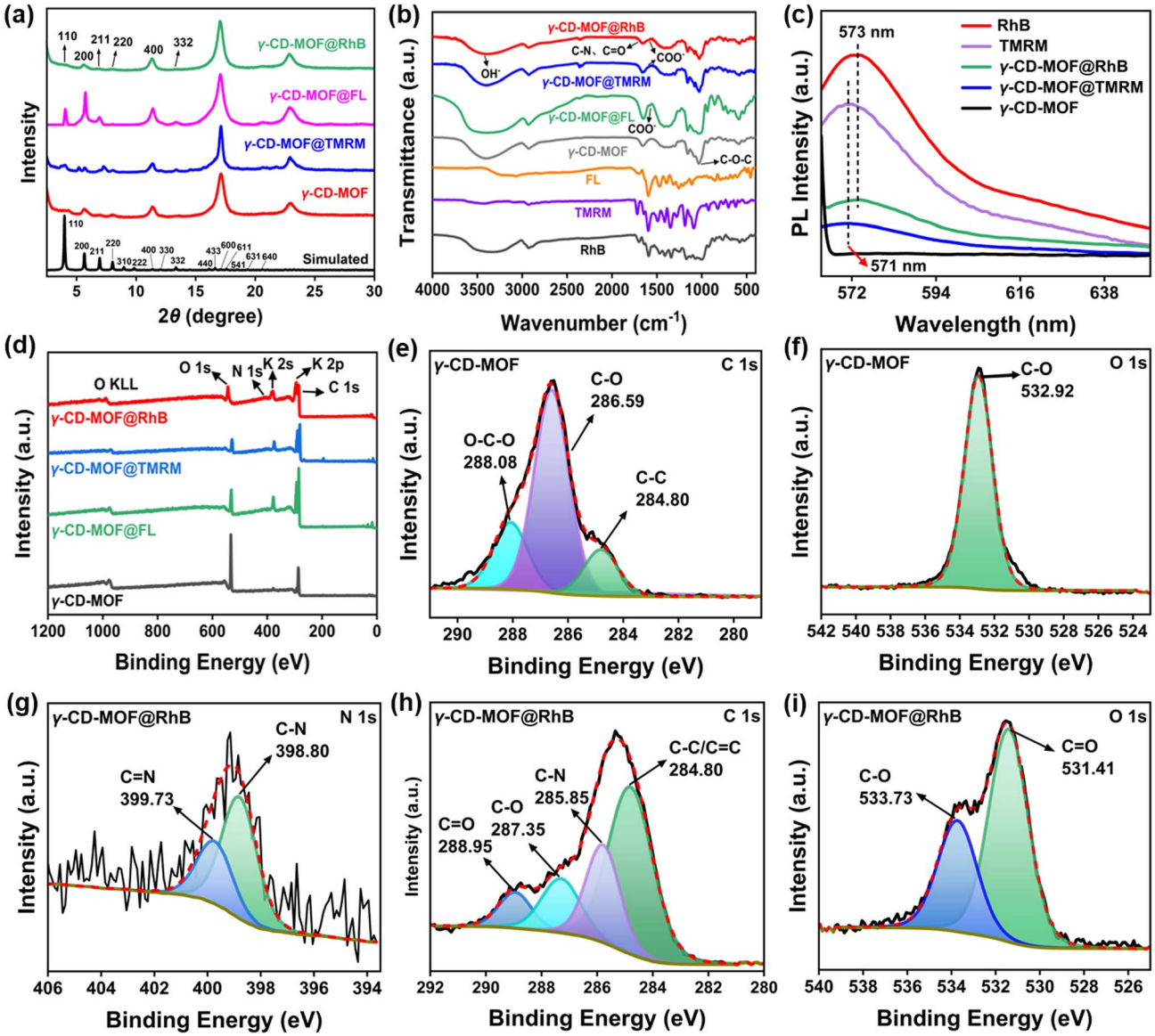

Fig. 3 (a–c) PXRD pattern, FT-IR plots and fluorescence spectra of γ-CD-MOF, γ-CD-MOF@RhB, γ-CD-MOF@TMRM, and γ-CD-MOF@FL. (d) XPS survey spectrum of γ-CD-MOF, γ-CD-MOF@RhB, γ-CD-MOF@TMRM, and γ-CD-MOF@FL. (e and f) C 1s, O 1s high-resolution XPS spectra of γ-CD-MOF. (g–i) N 1s, C 1s, O 1s high-resolution XPS spectra of γ-CD-MOF@RhB.

used to characterize the chemical bonds before and after the RhB, TMRM, and FL were encapsulated into γ-CD-MOF (Fig. 3b and S1†). The band at about 3300 cm^{-1} is attributed to the stretching vibration of –OH. After loading RhB, this vibration shifts to a shorter wave number, indicating the existence of hydrogen bonds.[35] The C–O–C stretching vibration peak of γ-CD-MOF is located around 1024 cm^{-1}.[36] More importantly, the absorption peak around 1590 cm^{-1} is assigned as the COO^- asymmetric stretching vibration of RhB, TMRM, or FL in γ-CD-MOF. The weak absorption peaks around 1695 cm^{-1} are attributed to the C=O stretching vibration of RhB, TMRM, or FL, and the weak absorption peaks around 1710 cm^{-1} are attributed to the C=N stretching vibration of RhB or TMRM, which indicates the low load of RhB, TMRM, and FL in γ-CD-MOF.[37] As shown in Fig. S5,† the N_2 adsorption–desorption isotherms of γ-CD-MOF and γ-CD-MOF@RhB indicated the presence of strong adsorption of N_2 at low relative pressure ($P/P_0 < 0.05$), suggesting that they are type I adsorption isotherms and have microporous structures. In addition, the BET surface area of the composites decreased from 1145.78 $m^2\ g^{-1}$ to 1119.60 $m^2\ g^{-1}$ after RhB loading, and the pore size distribution remained at 0.4–0.8 nm, which further indicated that the composites have a microporous structure (Fig. S5b†). As we know, when RhB is loaded into γ-CD-MOF, its nitrogen adsorption–desorption BET surface area decreases,[35] so the above results of the experiment are consistent with this regularity. In conclusion, the decrease in the nitrogen adsorption–desorption isotherm is attributed to the occupation of the cavity of γ-CD-MOF after loading RhB. The fluorescence spectrum was measured as shown in Fig. 3c and S6,† which shows that the corresponding fluorophores are

loaded in γ-CD-MOF. (The excitation wavelengths of RhB, TMRM, and FL are 556 nm, 549 nm, and 478 nm, respectively. The emission wavelengths of RhB, TMRM, and FL are 573 nm, 571 nm, and 516 nm, respectively.) Further, in order to verify the actual load of fluorophores in γ-CD-MOF, the fluorescence curves and calibration curves of RhB, TMRM, and FL are shown in Fig. S7–S9.† Subsequently, the fluorescence curves of composites with different feeding ratios are shown in Fig. S7f, S8f, and S9f,† which can estimate the actual load of RhB, TMRM, and FL in γ-CD-MOF according to the calibration curve (Table S1†). High-resolution X-ray photoelectron spectroscopy (XPS) was used to verify the chemical composition of the materials. As shown in Fig. 3d, the XPS survey spectra of γ-CD-MOF@RhB and γ-CD-MOF@TMRM display obvious N 1s absorption peaks compared to bare γ-CD-MOF and γ-CD-MOF@FL. Meanwhile, O 1s and K 2p peaks are present in all samples. The K–O absorption peaks of γ-CD-MOF, γ-CD-MOF@RhB, γ-CD-MOF@TMRM, and γ-CD-MOF@FL were observed at around 293 eV, indicating that K^+ formed coordination bonds with the hydroxide ions of γ-cyclodextrins. For γ-CD-MOF@RhB, there were three absorption peaks at 284.80, 287.35, and 288.95 eV in the C 1s spectrum, which are respectively attributed to the C–C, C–O (epoxy carbon), and O–C–O bonds of γ-CD-MOF, while the absorption peak at 285.85 eV was attributed to the C–N bond of RhB (Fig. 3h), which was not found in the bare γ-CD-MOF (Fig. 3e).[38–40] Compared to the bare γ-CD-MOF, the N 1s and O 1s spectra of γ-CD-MOF@RhB show the presence of C–N, C═N, C═O, and C–O bonds at 398.80, 399.73, 531.41, 533.73 eV, respectively, also indicating the successful loading of RhB (Fig. 3f, g and i).[41,42] In addition, the C–O peak is shifted to 287.35 eV after RhB is encapsulated, which further suggests the possible presence of hydrogen bond interactions. The XPS data of γ-CD-MOF@TMRM (Fig. S3a–c†) and γ-CD-MOF@FL (Fig. S4a and b†) are also consistent with γ-CD-MOF@RhB, indicating successful loading of TMRM and FL.

Gas sensing performance

As shown in Fig. 4a, the response of γ-CD-MOF toward 1000 ppm CO_2 was as low as 1.1 times (R_g/R_0) in a relatively dry environment (5% RH, N_2) due to the dramatic reduction of conducting ions such as protons and hydroxide ions in the relatively dry test environment. With a small amount of RhB loaded in γ-CD-MOF (γ-CD-MOF : RhB = 11.39 : 1), the response to 1000 ppm CO_2 rapidly increased to 1.68. When the RhB loading was increased to 2.25 : 1, the best CO_2 response was 2.24 (R_g/R_0), which was 2.04 times higher than that of the bare γ-CD-MOF. This should be attributed to the addition of carboxyl and amino groups when RhB was loaded, which endows the γ-CD-MOF to a higher level of ionic conductivity. Fig. 4b shows the characteristic curve of resistance change of γ-CD-MOF@RhB toward 1000 ppm CO_2. The resistance of the sensor sharply rises when exposed to CO_2 and returns to near baseline after the CO_2 is removed. The response time and recovery time of the sensor toward 1000 ppm CO_2 are 157 s and 487 s, respectively. Next, the sensing response of the sensor toward different concentrations of CO_2 was investigated. As shown in Fig. 4c, the CSPH ion channel-based sensor displays a monotonically increasing response and recovery toward CO_2 in the range of 10–1000 ppm. Interestingly, the CSPH ion channel-based sensor exhibits two linear fitting curves of response *vs.* CO_2 concentration, higher-slope linearity at lower concentration (10–100 ppm, 4.79×10^{-3} ppm^{-1}), and lower-slope linearity at higher concentration (200–1000 ppm CO_2, 7.91×10^{-4} ppm^{-1}), respectively. At low concentrations, the sensitivity arises only from the interaction of gas molecules at the surface of γ-CD-MOF, while at high concentrations, the sensitivity stems from the interaction of gas molecules both at the surface and inside the γ-CD-MOF, by which the sensing process becomes more complicated and time-consuming due to the bulk effect (Fig. 4c inset).[43]

Table 1 summarizes the CO_2 sensing performance of typical MOF-based chemiresistive CO_2 sensing materials.[22,23,44–50] The practical limit of detection (pLOD) of the CSPH ion channel-based sensor is 10 ppm, which is the lowest among the MOF-derived chemiresistive room temperature CO_2 sensors to date (Fig. 4c, Table 1). In addition, compared with other sensors, the CSPH ion channel-based sensor also exhibits excellent response value toward CO_2 ($R_g/R_0 = 1.50$, 100 ppm and $R_g/R_0 = 2.24$, 1000 ppm). As shown in Fig. 4d and e, the response curve of the CSPH ion channel-based sensor can maintain 5 cycles and has a stable response and recovery time, which means that it has excellent stability. The response value of the CSPH ion channel-based sensor toward 50 ppm CO_2 is 1.26 times, which is much higher than other interfering gases, including 50 ppm sulfur dioxide (SO_2), nitric oxide (NO), nitrogen dioxide (NO_2), carbon monoxide (CO), ammonia (NH_3), oxygen (O_2), hydrogen sulfide (H_2S), formaldehyde (HCHO), BTEX (benzene, toluene, ethylbenzene, and xylene), ethanol, and acetone (Fig. 4f). The concentration of the interfering gas that we detected was higher than that of human exhaled breath (approximately 15 ppb–1.75 ppm), which clearly demonstrates the selectivity of this CSPH ion channel sensor.[51–59] The high selectivity of the CSPH ion channel-based sensor is mainly attributed to the material having two CO_2 binding sites, including the hydroxide ion and the tertiary amines on RhB, which greatly increases the ability to interact with CO_2. In order to explore the effect of humidity, the CSPH ion channel-based sensor was placed at a relative humidity of 5–70% (RH), and then the response of 1000 ppm CO_2 was measured. The results show that the response value decreases with increasing humidity, which is attributed to the competition between H_2O and CO_2 adsorbed on the surface of the material (Fig. 4g and S10†). This problem can be solved by drying the target gas in advance.[60,61] The long-term stability of the CSPH ion channel-based sensor was investigated to verify its longevity in practical applications. It was found that even after four weeks, the sensing performance of the CSPH ion channel-based sensor had only decreased by 4%, demonstrating that the sensor has good long-term stability (Fig. 4h).

The effect on ion conduction behaviour was evaluated by comparing the ability of different types of functional groups to sense CO_2 (Fig. 4i). First of all, we have compared the gas sensing performance after loading RhB and TMRM containing tertiary amine into γ-CD-MOF. As a result, the response values of γ-CD-MOF@TMRM toward 1000 ppm CO_2 were similar to those of γ-CD-MOF@RhB at similar molar ratios. However, the

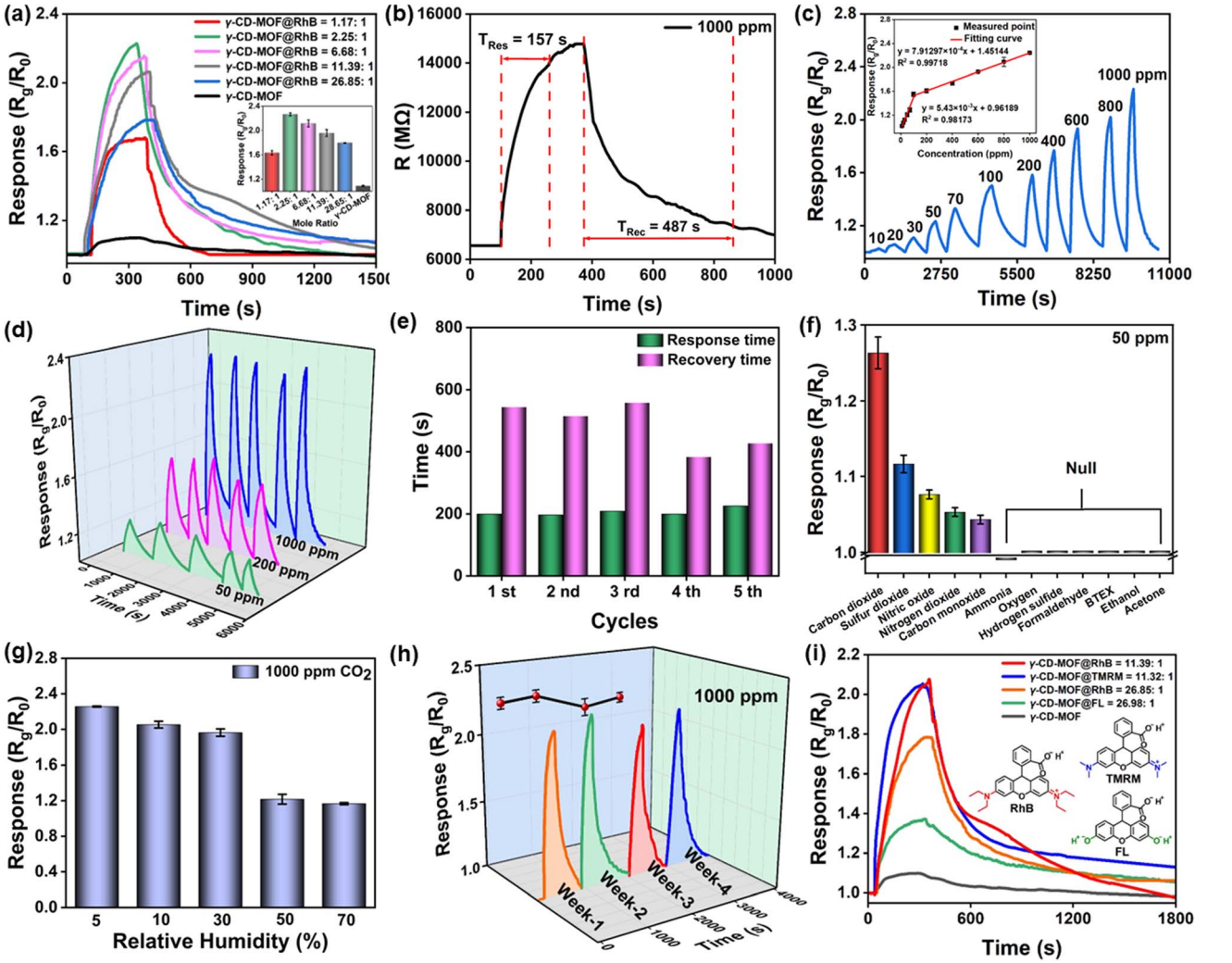

Fig. 4 (a) Sensing performance of γ-CD-MOF and RhB toward 1000 ppm CO_2 at different molar ratios. (b) Resistance response/recovery characteristics of γ-CD-MOF@RhB before and after exposure to 1000 ppm CO_2 under RT conditions. (c) Sensing performance and linear fitting curve for 10–1000 ppm CO_2. (d) Cycle curves toward 50, 200, and 1000 ppm CO_2. (e) Response and recovery times for each cycle toward 200 ppm CO_2. (f) The selectivity curve of the sensor for 50 ppm CO_2 and various interfering gases, including 50 ppm SO_2, NO, NO_2, CO, NH_3, O_2, H_2S, HCHO, BTEX (benzene, toluene, ethylbenzene, and xylene), ethanol, and acetone. (g) Sensing performance of the sensor to 1000 ppm CO_2 at a relative humidity of 5–70% RH. (h) Long-term stability curve of the sensor. (i) Comparison of sensing performance of RhB, TMRM, and FL with similar load in γ-CD-MOF toward 1000 ppm CO_2.

response values of γ-CD-MOF@FL were lower than those of γ-CD-MOF@RhB at similar molar ratios, which indicated the positive effect of the amine group. Furthermore, the alkaline dispersion of the material confirms that the ion conduction channels in γ-CD-MOF@RhB are dominated by hydroxide ions, possibly because the tertiary amines can react with water to produce more hydroxide ions prior to CO_2 exposure, facilitating an increase in the affinity of the sensing layer for CO_2 (Fig. S11†).[26] Therefore, a new hypothesis is proposed that there could be not only a proton conduction channel, but also hydroxide ion conduction channel in γ-CD-MOF@ RhB.

The commercial application potential of the sensor

To further verify the practical application potential of the sensor, the CSPH ion channel-based sensor is compared with the mature commercial infrared (IR) CO_2 meter. CSPH ion channel sensing material is integrated into the IDE, connected to the digital source meter with two wires and placed in a 1 L sealed test chamber (Fig. 5, lower right corner). When CO_2 is injected into the sealed test chamber, the digital source meter records the resistance change immediately. On the other hand, the commercial IR CO_2 meter was calibrated in a 5 L sealed test chamber, and subsequent readings at different concentrations of CO_2 were recorded (Fig. 5, top left corner, Fig. S12 and S13†). The reading of the CSPH ion channel-sensor at different concentrations of CO_2 is very close to the commercial IR CO_2 meter, as well as the value of actual injected CO_2 (Table S2†). In addition, the correlation between CSPH ion channel-based sensor and commercial IR CO_2 meters was compared at different CO_2 concentrations. The results show that the

Table 1 Summary of CO_2 sensing performance of MOF-based materials based on electrical signals

Materials	Operating temperature	Sensing mechanism	D_R[a] (ppm)	Response[b]	t_{res}/t_{rec}	Ref.
γ-CD-MOF-2	80 °C at recovery	Proton conduction	100 000–1 000 000	~550-fold, 1 000 000 ppm	300 s/2400 s	22
γ-CD-MOF-1	R.T.	Proton conduction	1 000 000	1/50 of the baseline 1 000 000 ppm	3 s/10 s	23
NH_2-UiO-66 (Zr)	150 °C	Lewis acid–base reaction	5000	1.13 (5000 ppm)[ε]	About 50 s/75 s	44
SnO_2@ZIF-67	205 °C	Oxidation reaction	500–5000	1.20, 5000 ppm[ε]	Less than 30 s/30 s	45
GA@UiO-66-NH_2	200 °C	Lewis acid–base reaction	50 000–1 000 000	1.04, 50 000 ppm[ε]	18 s/18 s	46
Cu_3(HIB)$_2$	R.T.	Lewis acid–base reaction	400–2500	0.62% (100 ppm)$^{-1}$[δ]	420 s/600 s	47
Co-MOF-74-TTF	R.T.	Lewis acid–base reaction	1 000 000	—	200 s/—	48
Zn-MOF-74	R.T.	Lewis acid–base reaction	500–2000	1.25, 1000 ppm[ζ]	180 min/180 min	49
		Proton conduction				
MIL-53(Al)/CB (carbon black)	R.T.	Breathing effect of MIL-53	1 000 000	1.15 at 20 bar CO_2, 1 000 000 ppm[ζ]	Less than 30 s	50
γ-CD-MOF@RhB	**R.T.**	**CO_2-switched CSPH ion channel**	**10–1000**	**1.50, 100 ppm**	**157 s/487 s**	**This work**
				2.24, 1000 ppm[ζ]		

[a] D_R represents the concentration range of the practical study. [b] For ease of comparison, the evaluation of response is converted as ε: response = R_a/R_g, δ: response = G/G_0 (G_0 = initial baseline current) and ζ: response = R_g/R_0.

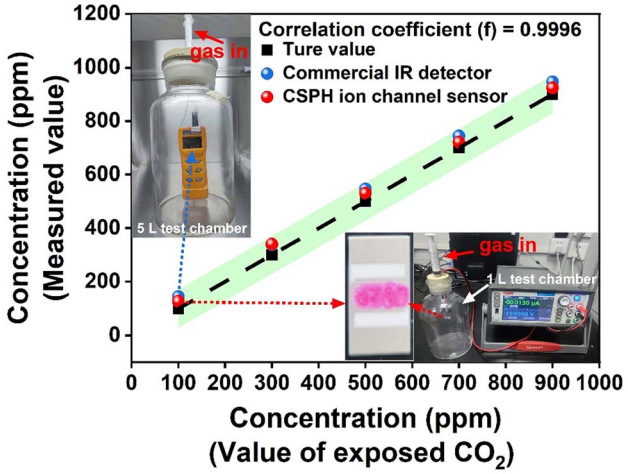

Fig. 5 Comparing the correlation between our sensor and commercial IR detector, the illustration in the upper corner shows the measurement process of commercial IR detector, while the lower right corner shows our sensor.

correlation coefficient of CO_2 concentration between the CSPH ion channel-based sensor and the commercial IR CO_2 meter is 0.9996, which means that the CSPH ion channel-based sensor has excellent accuracy and reliability (Fig. 5). Further, the CSPH ion channel-based sensor demonstrates a real-time detection capability, which means that the sensors have great potential for applications (Fig. S14†).

The detection of the sensor on CO_2 exhalation from the human body

Pulmonary abnormalities, including carbon monoxide diffusion (D_{LCO}) abnormalities and respiratory disorders, could persist long after the recovery from COVID-19 infection.[8–10] These abnormalities may cause CO_2 to not be discharged smoothly from the body. Therefore, it is possible to assess whether there is abnormal lung function by analyzing the exhaled CO_2 of people who have recovered from COVID-19. A simple silica gel drying device was used to solve the humidity problem of human exhaled breath by connecting the two ends of a drying unit to a syringe and gas collection bags containing human exhaled breath (Fig. S15†). When the gas was collected using syringes, the human exhaled flow was dried after passing through the drying unit. The total time from the gas collection process (including drying, extraction, and injection) to complete the gas detection process is 800 ± 147 s (Fig. S16†). The CSPH ion channel-based sensor is used to detect human exhalation after drying, including the exhalation of COVID-19 rehabilitative volunteers and undiseased volunteers. The results showed that the exhaled CO_2 of the COVID-19 rehabilitative volunteers and the undiseased individuals could be clearly distinguished, with the exhaled CO_2 average concentration of the COVID-19 rehabilitative volunteers (R_g/R_0 = 1.45), being around 14.48% lower than that of the undiseased individuals (R_g/R_0 = 1.66), logically indicating that some rehabilitators would still have pulmonary abnormalities causing CO_2

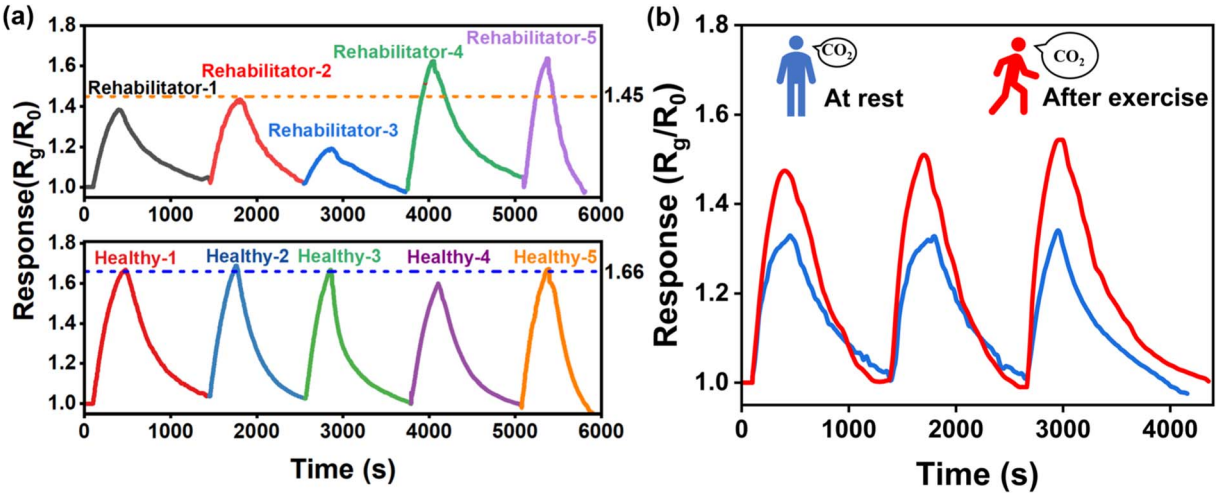

Fig. 6 (a) Detection of human exhaled CO_2, including those COVID-19 rehabilitative volunteers (rehabilitator 1–5) and undiseased individuals (healthy 1–5); the dashed line represents the average value. (b) Detection of human exhaled CO_2 at rest (blue curve) and after walking for 30 min (red curve).

not to be properly expelled from the body (Fig. 6a, Table S3†). This result suggests that the CSPH ion channel-based sensor has potential for large-scale application in assessing cardiopulmonary function. In addition, Fig. 6b shows the comparison of CO_2 exhaled by the human body at rest and after exercise (walking for 30 min). The results showed that the average concentration of human exhaled CO_2 after exercise was around 12.78% higher than before exercise, which clearly shows that the CO_2 concentration in exhalation is related to the metabolism of the human body.[62,63] The above evidence suggests that this bio-inspired CSPH ion channel chemiresistive sensor has great potential for application in monitoring human exhalation.

Mechanism of ion-conduction

It can be assumed that both the H^+ ion conduction channel and OH^- ion conduction channel exist in γ-CD-MOF@RhB (Fig. 4i, S11†). To further confirm the ion conduction mechanism of γ-CD-MOF@RhB, the electromotive force (EMF) was used to measure the ion conduction species. A water vapor concentration difference cell is created by blowing a dry nitrogen gas stream on one side of the sheet and a humid gas stream (50% RH) on the other side to create a concentration difference, where the open circuit voltage is the EMF of the ions migrating through the material, and its sign represents the ion conduction species.[64,65] Firstly, γ-CD-MOF@RhB was heated in an oven at 80 °C for 5 h to remove water and CO_2. Before CO_2 injection, the EMF value of γ-CD-MOF@RhB was negative, which was attributed to the conduction of hydroxide ions. When exposed to CO_2 for 15 min, the EMF value changed to positive values, indicating a switch in the ion conduction channels. It can be explained that the binding of basic hydroxide ions to CO_2 leads to the inhibition of hydroxide ion channels, with the result that proton conduction dominates. The EMF value of the sheet became negative when the CO_2 was removed by heating at 80 °C for 5 h, which means that the proton ion conduction in the system switched back to hydroxide ion conduction after the CO_2 was removed (Fig. 7a). This mode is similar to the pH-induced switching of H^+ and OH^- on graphene oxide reported by Fukuda *et al.* in 2020, suggesting that there could also be a CO_2-induced switching of H^+/OH^- within γ-CDMOF@RhB.[66] To further verify the switching ability of the H^+/OH^- ion conduction channel, the change in resistance from 0 to 1 000 000 ppm CO_2 was measured at a dynamic flow rate of 50 mL min^{-1} (Fig. 7b). The results show that prior to CO_2 exposure, hydroxide ion-conduction is dominant owing to the presence of large amounts of hydroxide ions in the material. After exposure to CO_2, there is an upward slope in the resistance curve of the material, which is attributed to the consumption of hydroxide ions in combination with CO_2, resulting in a sharp increase in resistance. After 73 s (approximately 60 000 ppm CO_2), an inflection point in the resistance curve occurs, which is attributed to the consumption of hydroxide ions reaching the limit and the ion conduction channel switch opening, leading to the dominance of proton conduction, resulting in a downward increase in the resistance curve. Then, the resistance of the CSPH ion channel-based sensor reaches equilibrium at 1653 s (approximately 1 000 000 ppm CO_2). Finally, after the removal of CO_2, the resistance curve bends again owing to the release of hydroxide ions to dominate the ion conduction channel. Hence, in this cycle, CO_2 could be acting as a switch, controlling the opening and closing of channels for ion conduction.

Electrochemical impedance spectroscopy (EIS) was measured to study the proton conduction behavior of the sensor after injecting CO_2 at 70% RH. As shown in Fig. 7c, after loading RhB into γ-CD-MOF, the ion conductivity σ changes from 7.51 $\times$ 10^{-12} S cm^{-1} to 5.00 $\times$ 10^{-11} S cm^{-1}, which is 6.66 times higher ($\sigma = l/RA$, l and A are the thickness and cross-sectional area of the tablet, and R is the resistance). These results further explain the positive contribution of RhB to the enhancement of ionic conductivity, which could be attributed to the formation of hydroxyl ion channels and a broader

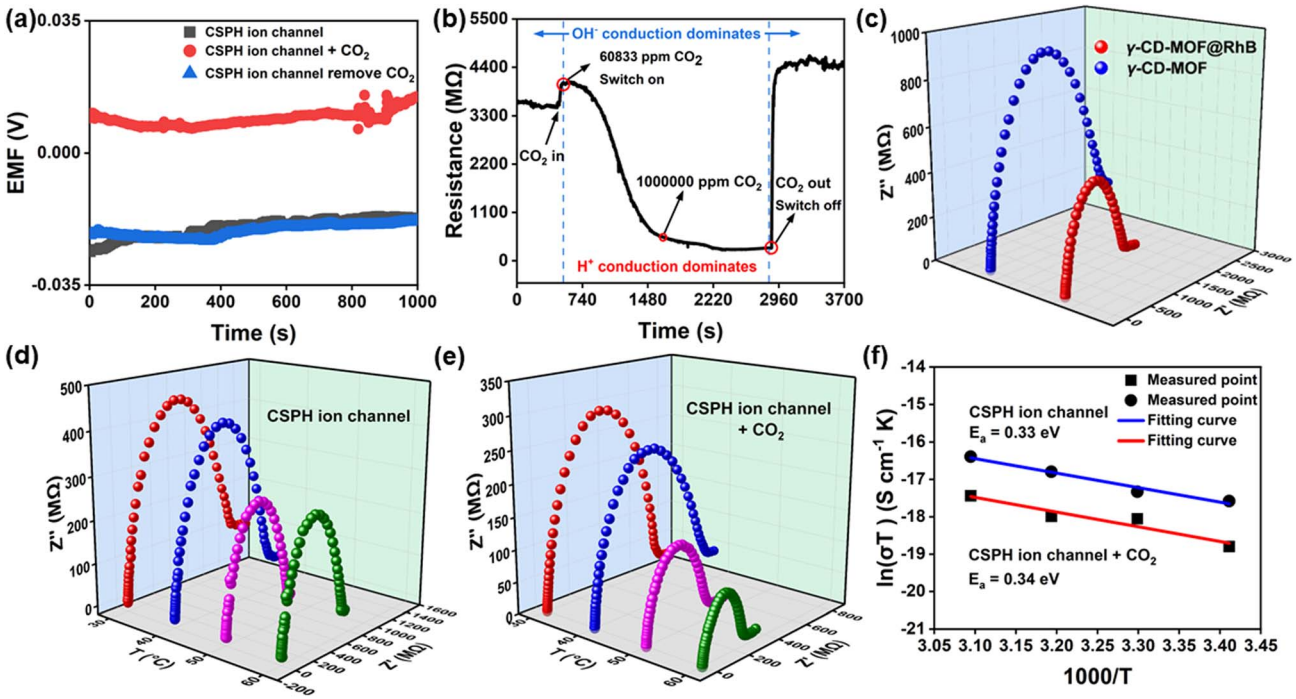

Fig. 7 (a) EMF of γ-CD-MOF@RhB. (b) Comparison of the resistance change of γ-CD-MOF@RhB from 0 to 1 000 000 ppm CO_2 at 50 mL min^{-1} flow rate. (c) Comparison of Nyquist plots between γ-CD-MOF and γ-CD-MOF@RhB. (d) Nyquist plots of γ-CD-MOF@RhB at 30–60 °C. (e) Nyquist plot of γ-CD-MOF@RhB after exposure to CO_2 for 15 min at 30–60 °C. (f) Arrhenius curve of γ-CD-MOF@RhB.

hydrogen bonding network.[67,68] As shown in the Nyquist plot (Fig. 7d), the impedance of γ-CD-MOF@RhB decreases with increasing temperature in the range of 30–60 °C prior to CO_2 exposure. Fig. 7e shows the Nyquist plot of γ-CD-MOF@RhB after exposure to CO_2 for 15 min. The decrease in impedance values compared to those before CO_2 exposure is due to the

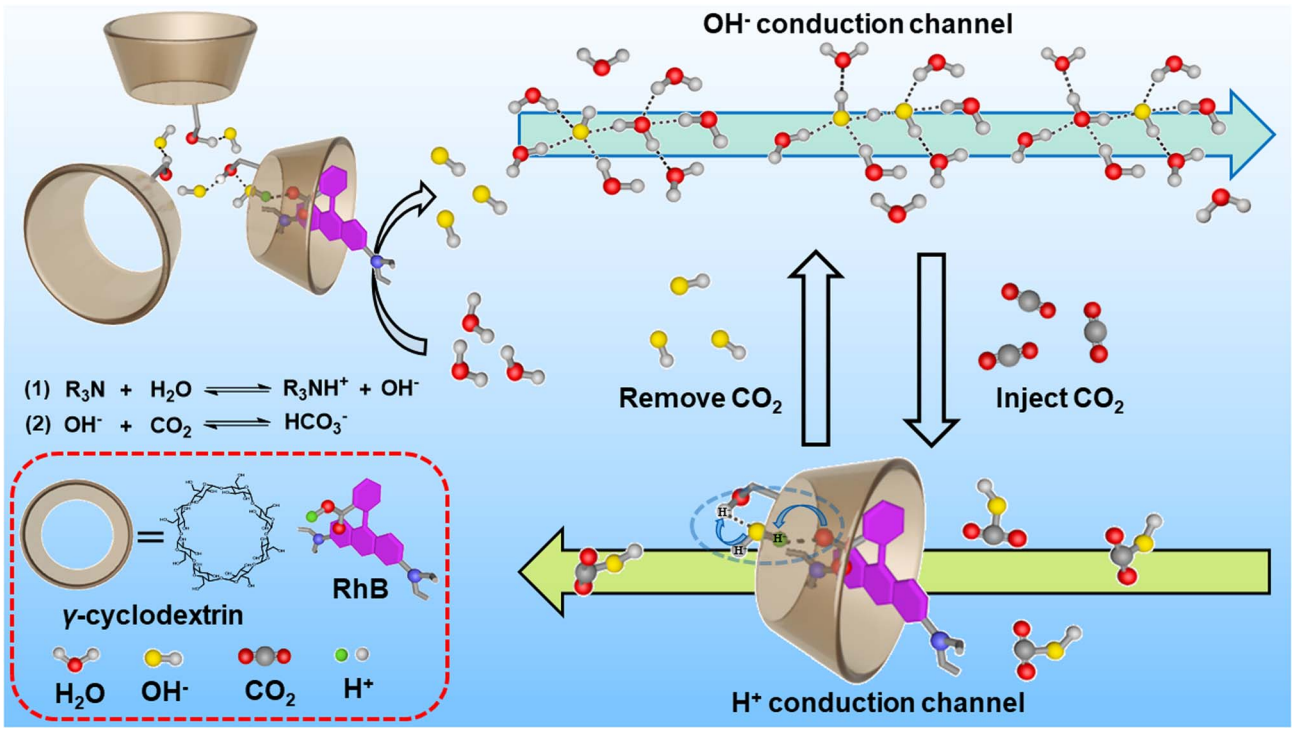

Fig. 8 Sensing mechanism of the CSPH ion channel-based sensor.

large depletion of hydroxide ions, allowing proton conduction with higher ion mobility to dominate. Fig. 7f shows the Arrhenius curve of γ-CD-MOF@RhB at 30–60 °C. The activation energy before and after exposure to CO_2 are $E_a = 0.33$ eV and $E_a = 0.34$ eV, respectively. These results show that hydroxyl ion conduction and proton conduction both follow Grotthuss mechanisms ($E_a < 0.4$ eV).[69–73]

CO_2 sensing mechanism of the CSPH ion channel-based sensor

Recent studies have shown that the adsorption mechanism of γ-CD-MOF and CO_2 may be due to the combination of hydroxyl counterions with CO_2, not only the hydroxyl sites on the γ-CDs.[28] In addition, the γ-CD-MOF has a cubic structure, which means that every three γ-CDs form a triangular-shaped β-window. There are secondary hydroxyl groups in the triangular-shaped β-window that can form hydrogen bonds with the hydroxide ions.[73] As shown in Fig. 8, there are mutually switchable proton ion conduction and hydroxide ion conduction in the CSPH ion channel. The tertiary amine on RhB can combine with hydrogen ions of water, releasing a large number of hydroxide ions. These hydroxide ions form a stable four-water molecule structure $OH^-(H_2O)_4$ with water.[69] The inert resultant $OH^-(H_2O)_4$ is then converted into an activated $OH^-(H_2O)_3$ structure, which causes the hydroxide ion to form a hydrogen bond with the hydrogen atom of the neighboring water and initiate a proton transfer, resulting in the formation of new stable $OH^-(H_2O)_4$. Eventually, the hydroxide ions are transferred along this network. When the CSPH ion channel is exposed to CO_2, hydroxide ions combine with CO_2 in a large amount to form bicarbonate species with slow ion migration, resulting in a sharp decline in the number of hydroxide ions, and the interference of hydroxide ion conduction channels, resulting in the switching of hydroxide ion conduction channels to hydrogen ion-conduction channels. Furthermore, the dispersion of the material is alkaline (Fig. S11†), indicating that the hydroxide ion is the dominant migration species, and there is no doubt that its reduction leads to a sharp increase in the resistance of the material. In addition, tertiary amine also provides additional CO_2 binding sites in the presence of water.[27,28] The H^+ of the carboxyl group from RhB is captured by basic hydroxide ions, and then these hydroxide ions form hydrogen bonds with the hydroxyl group on γ-CD to realize proton hopping (Grotthuss mechanism, Fig. 7f).[73] When CO_2 is removed, due to the release of hydroxide ions, the ion conduction channel is again dominated by hydroxide ions. A cycle in which CO_2 acts as a switch for the ion-conduction channels is thus completed.

Conclusions

In summary, we have constructed the first bio-inspired CO_2-switchable H^+/OH^- ion channel (CSPH ion channel) and fabricated a room-temperature chemiresistive CO_2 sensor based on this ion channel. The switching characteristics of this ion channel are similar to the reversible activation mechanism of the SLAC1 in plant stomatal guard cells induced by CO_2 during photosynthesis, which is beneficial to improve the understanding of the SLAC1 and even the gated gas adsorption process in photosynthesis and provide new ideas for the preparation of bionic artificial CO_2-switched ion channels. The ultra-low detection limit (pLOD) of 10 ppm and high sensitivity ($R_g/R_0 = 1.50$, 100 ppm) of the sensor can be used for human exhaled CO_2 detection applications. The results show that the sensor successfully differentiates human exhaled CO_2 before and after exercise and assesses cardiopulmonary function after COVID-19 recovery. This work provides a deeper insight into plant photosynthesis and a new approach to developing bionic artificial CO_2-switched ion channels for room temperature CO_2 sensing.

Conflicts of interest

The authors declare no competing financial interest.

Acknowledgements

This work was supported by the National Natural Science Foundation of China (Grant No. 51973070), Science and Technology Program of Guangzhou (No. 2019050001), Guangdong Basic and Applied Basic Research Foundation (2022A1515010577 and 2021A1515012420), Innovative Team Project of Education Bureau of Guangdong Province (2018KCXTD009), Guangdong Science and Technology Project-International Cooperation (2022A0505050069), Start-up Foundation from SCNU, Guangdong Provincial Key Laboratory of Optical Information Materials and Technology (No. 2017B030301007), MOE International Laboratory for Optical Information Technologies, and the 111 Project, Science and Technology Innovation Strategy Special Foundation of Guangdong (No. pdjh2023b0144). The calculations were performed at Bianshui Riverside Supercomputing Center (BRSC).

References

1 V. Leivo, T. Prasauskas, L. Du, M. Turunen, M. Kiviste, A. Aaltonen, D. Martuzevicius and U. Haverinen-Shaughnessy, *Sci. Total Environ.*, 2018, **621**, 398.
2 M. Struzik, I. Garbayo, R. Pfenninger and J. L. M. Rupp, *Adv. Mater.*, 2018, **30**, 44.
3 A. Gheorghe, O. Lugier, B. Ye and S. Tanase, *J. Mater. Chem. C*, 2021, **9**, 16132.
4 A. Libanori, G. Chen, X. Zhao, Y. Zhou and J. Chen, *Nat. Electron.*, 2022, **5**, 142.
5 Y. Su, G. Chen, C. Chen, Q. Gong, G. Xie, M. Yao, H. Tai, Y. Jiang and J. Chen, *Adv. Mater.*, 2021, **33**, 2101262.
6 M. J. Donald and B. Paterson, *Emerg. Med. J.*, 2006, **23**, 728.
7 H. Aminiahidashti, S. Shafiee, A. Kiasari and M. Sazgar, *Emergency*, 2018, **6**, e5.
8 Y. Gao, R. Chen, Q. Geng, X. Mo, C. Zhan, W. Jian, S. Li and J. Zheng, *Eur. Respir. J.*, 2021, **57**, 2004265.
9 C. B. Ingul, A. Edvardsen, T. Follestad, D. Trebinjac, O. A. W. Ankerstjerne, E. Bronstad, O. Rasch-Halvorsen,

B. Aarli, H. Dalen, B. M. Nes, T. V. Lerum, G. Einvik, K. Stavem and I. Skjorten, *Eur. Respir. J.*, 2023, **61**, 2200745.
10 L. Heydemann, M. Ciurkiewicz, G. Beythien, K. Becker, K. Schughart, S. Stanelle-Bertram, B. Schaumburg, N. Mounogou-Kouassi, S. Beck, M. Zickler, M. Kuhnel, G. Gabriel, A. Beineke, W. Baumgartner and F. Armando, *Nat. Commun.*, 2023, **14**, 3267.
11 M. Liu, R. M. M. Gray, L. Costa, C. R. R. Markus, A. Roy and A. Marandi, *Nat. Commun.*, 2023, **14**, 1044.
12 S. Moumen, I. Raible, A. Krauß and J. Wöllenstein, *Sens. Actuators, B*, 2016, 1083.
13 P. Moreno-Garcia, N. Kovacs, V. Grozovski, M. D. J. Galvez-Vazquez, S. Vesztergom and P. Broekmann, *Anal. Chem.*, 2020, **92**, 4301.
14 B. Li, H. Wu, C. Feng, S. Jia and L. Dong, *Anal. Chem.*, 2023, **95**, 6138.
15 Y. Li, X. Wu, B. Yang, X. Zhang, H. Li, A. Umar, N. F. de Rooij, G. Zhou and Y. Wang, *ACS Appl. Mater. Interfaces*, 2019, **11**, 37077.
16 Z. Mai, H. Li, Y. Gao, Y. Niu, Y. Li, N. F. de Rooij, A. Umar, M. S. Al-Assiri, Y. Wang and G. Zhou, *Analyst*, 2020, **145**, 3528.
17 C. A. Zito, T. M. Perfecto, A.-C. Dippel, D. P. Volanti and D. Koziej, *ACS Appl. Mater. Interfaces*, 2020, **12**, 17757.
18 S. Kanaparthi and S. G. Singh, *ACS Appl. Nano Mater.*, 2019, **2**, 700.
19 R. A. Smaldone, R. S. Forgan, H. Furukawa, J. J. Gassensmith, A. M. Z. Slawin, O. M. Yaghi and J. F. Stoddart, *Angew. Chem.*, 2010, **49**, 8630.
20 J. J. Gassensmith, H. Furukawa, R. A. Smaldone, R. S. Forgan, Y. Y. Botros, O. M. Yaghi and J. F. Stoddart, *J. Am. Chem. Soc.*, 2011, **133**, 15312.
21 D. Wu, J. J. Gassensmith, D. Gouvea, S. Ushakov, J. F. Stoddart and A. Navrotsky, *J. Am. Chem. Soc.*, 2013, **135**, 6790.
22 J. J. Gassensmith, J. Y. Kim, J. M. Holcroft, O. K. Farha, J. F. Stoddart, J. T. Hupp and N. C. Jeong, *J. Am. Chem. Soc.*, 2014, **136**, 8277.
23 D. Shen, G. Wang, Z. Liu, P. Li, K. Cai, C. Cheng, Y. Shi, J.-M. Han, C.-W. Kung, X. Gong, Q.-H. Guo, H. Chen, A. C. H. Sue, Y. Y. Botros, A. Facchetti, O. K. Farha, T. J. Marks and J. F. Stoddart, *J. Am. Chem. Soc.*, 2018, **140**, 11402.
24 Y. Xu, M. Zhang, T. Tian, Y. Shang, Z. Meng, J. Jiang, J. Zhai and Y. Wang, *NPG Asia Mater.*, 2015, **7**, e215.
25 Q.-S. Du, X.-W. Fan, C.-H. Wang and R.-B. Huang, *PLoS One*, 2011, **6**, e24264.
26 H. J. de Boer, M. B. Eppinga, M. J. Wassen and S. C. Dekker, *Nat. Commun.*, 2012, **3**, 1221.
27 T. L. Donaldson and Y. N. Nguyen, *Ind. Eng. Chem. Fundam.*, 1980, **19**, 260–266.
28 M. E. Zick, S. M. Pugh, J.-H. Lee, A. C. Forse and P. J. Milner, *Angew. Chem.*, 2022, **61**, e202206718.
29 L. Hu, K. Li, W. Shang, X. Zhu and M. Liu, *Angew. Chem.*, 2020, **59**, 4953.
30 Y. Chen, B. Yu, Y. Cui, S. Xu and J. Gong, *Chem. Mater.*, 2019, **31**, 1289.
31 Y. Gao, J. Wang, Y. Feng, N. Cao, H. Li, N. F. de Rooij, A. Umar, P. J. French, Y. Wang and G. Zhou, *Small*, 2022, **18**, 2103259.
32 H. Liang, L. Guo, N. Cao, H. Hu, H. Li, N. Frans de Rooij, A. Umar, H. Algarni, Y. Wang and G. Zhou, *J. Mater. Chem. A*, 2021, **9**, 23955.
33 H. Liang, X. Guo, L. Guo, S. Liu, Q. Zhan, H. Yang, H. Li, N. F. de Rooij, Y.-K. Lee, P. J. French, Y. Wang and G. Zhou, *Adv. Funct. Mater.*, 2023, **33**, 2215099.
34 Y. Chang, M. Chen, Z. Fu, R. Lu, Y. Gao, F. Chen, H. Li, N. F. de Rooij, Y.-K. Lee, Y. Wang and G. Zhou, *J. Mater. Chem. A*, 2023, **11**, 6966.
35 M. Peng, A. M. Kaczmarek and K. Van Hecke, *ACS Appl. Mater. Interfaces*, 2022, **14**, 14367.
36 Y. Furukawa, T. Ishiwata, K. Sugikawa, K. Kokado and K. Sada, *Angew. Chem.*, 2012, **51**, 10566.
37 R. M. Dukali, I. M. Radovic, D. B. Stojanovic, D. M. Sevic, V. J. Radojevic, D. M. Jocic and R. R. Aleksic, *J. Serb. Chem. Soc.*, 2014, **79**, 867.
38 F. Luan, Y. Wang, S. Zhang, X. Zhuang, C. Tian, X. Fu and L. Chen, *Analyst*, 2020, **145**, 1943.
39 Z.-J. Qiu, S.-T. Fan, C.-Y. Xing, M.-M. Song, Z.-J. Nie, L. Xu, S.-X. Zhang, L. Wang, S. Zhang and B.-J. Li, *ACS Appl. Mater. Interfaces*, 2020, **12**, 55299.
40 S. Li, X. Hu, S. Chen, X. Wang, H. Shang, Y. Zhou, J. Dai, L. Xiao, W. Qin and Y. Liu, *Food Hydrocolloids*, 2023, **136**, 108294.
41 J. Che, K. Chen, J. Song, Y. Tu, O. O. Reymick, X. Chen and N. Tao, *Curr. Res. Food Sci.*, 2022, **5**, 2114.
42 J. Peng, J. Huang, Y. Peng, Y. Xiao and M. Yang, *Surf. Coat. Technol.*, 2022, **451**, 129064.
43 Y. Zhou, Y. Wang, Y. Wang and X. Li, *Anal. Chem.*, 2020, **92**, 16033.
44 M. E. DMello, N. G. Sundaram, A. Singh, A. K. Singh and S. B. Kalidindi, *Chem. Commun.*, 2019, **55**, 349.
45 M. E. DMello, N. G. Sundaram and S. B. Kalidindi, *Chem.–Eur. J.*, 2018, **24**, 9220.
46 K. Jayaramulu, M. Esclance Dmello, K. Kesavan, A. Schneemann, M. Otyepka, S. Kment, C. Narayana, S. B. Kalidindi, R. S. Varma, R. Zboril and R. A. Fischer, *J. Mater. Chem. A*, 2021, **9**, 17434.
47 I. Stassen, J.-H. Dou, C. Hendon and M. Dinca, *ACS Cent. Sci.*, 2019, **5**, 1425.
48 I. Strauss, A. Mundstock, M. Treger, K. Lange, S. Hwang, C. Chmelik, P. Rusch, N. C. Bigall, T. Pichler, H. Shiozawa and J. Caro, *ACS Appl. Mater. Interfaces*, 2019, **11**, 14175.
49 B. Ye, A. Gheorghe, R. van Hal, M. Zevenbergen and S. Tanase, *Mol. Syst. Des. Eng.*, 2020, **5**, 1071.
50 P. Freund, L. Mielewczyk, M. Rauche, I. Senkovska, S. Ehrling, E. Brunner and S. Kaskel, *ACS Sustain. Chem. Eng.*, 2019, **7**, 4012.
51 M. A. Berry, D. E. Shaw, R. H. Green, C. E. Brightling, A. J. Wardlaw and I. D. Pavord, *Clin. Exp. Allergy*, 2005, **35**, 1175.
52 A. Shanmugasundaram, S. V Manorama, D.-S. Kim, Y.-J. Jeong and D. Weon Lee, *Chem. Eng. J.*, 2022, 137736.

53 L. Li, L. Zhou, Z. Hu, T. Li, B. Chen, H.-Y. Li and H. Liu, *ACS Appl. Mater. Interfaces*, 2023, **15**, 15707.
54 L. Fu, D. Li and W. Tang, *J. Alloys Compd.*, 2023, **960**, 170648.
55 J. Zhao, H. He, J. Guo, Z. He, C. Zhao, H. Wang, Z. Gao and Y.-Y. Song, *ACS Sens.*, 2023, **8**, 2824.
56 A. A. Pereira, S. L. Pollard, R. Locke, K. Romero, J. J. Lima, N. N. Hansel and W. Checkley, *Respir. Med.*, 2018, **145**, 212.
57 H. Morimatsu, T. Takahashi, T. Matsusaki, M. Hayashi, J. Matsumi, H. Shimizu, M. Matsumi and K. Morita, *J. Breath Res.*, 2010, **4**, 047103.
58 T. Hibbard, K. Crowley, F. Kelly, F. Ward, J. Holian, A. Watson and A. J. Killard, *Anal. Chem.*, 2013, **85**, 12158.
59 P. Srinivasan, K. Dhingra and K. Kailasam, *J. Mater. Chem. A*, 2023, **11**, 17418.
60 J. Wang, Y. Gao, F. Chen, L. Zhang, H. Li, N. F. de Rooij, A. Umar, Y.-K. Lee, P. J. French, B. Yang, G. Zho and Y. Wang, *ACS Appl. Mater. Interfaces*, 2022, **14**, 53193.
61 P. E. Silkoff, M. Carlson, T. Bourke, R. Katial, E. Ogren and S. J. Szefler, *J. Allergy Clin. Immunol.*, 2004, **114**, 1241.
62 J. Gong, M. Antonietti and J. Yuan, *Angew. Chem.*, 2017, **56**, 7557.
63 H. Wang, C. O. Ogolla, G. Panchal, M. Hepp, S. Delacroix, D. Cruz, D. Kojda, J. Ciston, C. Ophus, A. Knop-Gericke, K. Habicht, B. Butz and V. Strauss, *Adv. Funct. Mater.*, 2022, **32**, 2207406.
64 P. Sun, R. Ma, X. Bai, K. Wang, H. Zhu and T. Sasaki, *Sci. Adv.*, 2017, **3**, e1602629.
65 K. Tadanaga, Y. Furukawa, A. Hayashi and M. Tatsumisago, *Adv. Mater.*, 2010, **22**, 4401.
66 M. Fukuda, S. Islam, Y. Shudo, J. Yagyu, L. F. Lindoy and S. Hayami, *Chem. Commun.*, 2020, **56**, 4364.
67 Y. Zhou, Y. Xiao and J. Zhao, *New J. Chem.*, 2020, **44**, 16062.
68 S. Guo, Z. Zou, Y. Chen, X. Long, M. Liu, X. Li, J. Tan and R. Chen, *Environ. Pollut.*, 2023, **320**, 121060.
69 W. Xue, C. D. Sewell, Q. Zhou and Z. Lin, *Angew. Chem.*, 2022, **61**, e202206512.
70 W. H. Ho, S.-C. Li, Y.-C. Wang, T.-E. Chang, Y.-T. Chiang, Y.-P. Li and C.-W. Kung, *ACS Appl. Mater. Interfaces*, 2021, **13**, 55347.
71 P. Ramaswamy, N. E. Wong and G. K. H. Shimizu, *Chem. Soc. Rev.*, 2014, **43**, 5913.
72 S. C. Pal and M. C. Das, *Adv. Funct. Mater.*, 2021, **31**, 2101584.
73 H. D. M. Pham and R. Z. Khaliullin, *J. Phys. Chem. C*, 2021, **125**, 24719.